EES Solar

PAPER

View Article Online
View Journal

Cite this: DOI: 10.1039/d6el00034g

Characterization of ionic–electronic transport and recombination in perovskite solar cells under multi-biasing conditions

Juan Pablo Medina Flechas, *[ab] Dounya Barrit, [ab] Raj Dashrath Patel, [b] Tianfang Li, [ab] Estelle Cariou, [b] Marion Provost, [b] Leonardo Koprio, [bc] Sylvain Le Gall, [bcd] Jean-Paul Kleider, [bcd] Osbel Almora, [e] Camille Bainier, [ab] Pilar López-Varo *[b] and Philip Schulz *[bf]

Perovskite solar cells (PSCs) are among the most promising photovoltaic technologies, offering high efficiencies and low fabrication costs. However, their commercialization remains limited by stability issues and incomplete understanding of the intrinsic mechanisms governing device performance. In particular, slow mobile-ion dynamics can modulate charge recombination and extraction, strongly affecting device operation. Here, we use impedance spectroscopy (IS) to investigate the underlying processes that govern the current–voltage (J–V) response of PSCs under operational conditions. To this end, we combine J–V, Suns-V_{oc} and IS measurements using a multi-bias approach to analyze p–i–n PSCs under short-circuit (SC) and open-circuit (OC) conditions over a wide range of illumination intensities. Complementarily, drift-diffusion (DD) simulations and equivalent circuit model (ECM) analysis of IS under SC conditions enable extraction of key transport properties, including carrier mobilities, mobile ion concentration, and shunt resistance. The role of mobile ion concentration is analyzed for both regimes. Across the simulated parameter space, the low-frequency dark resistance is determined by the shunt resistance and nearly independent of recombination rates or mobile ion concentration. Therefore, the associated dark low-frequency RC time constant cannot be directly interpreted as a recombination lifetime. Under OC conditions, we further evaluate the coupled effects of ionic motion and energy band offsets on recombination, comparing the ideality factor derived across techniques. This integrated experimental–theoretical framework provides deeper insight into the electronic and ionic processes governing PSC performance.

Received 20th February 2026
Accepted 5th May 2026

DOI: 10.1039/d6el00034g

rsc.li/EESSolar

Broader context

Perovskite solar cells (PSCs) hold immense promise for next-generation photovoltaic technologies, offering high efficiency and cost-effective manufacturing. However, their widespread deployment is hindered by fundamental challenges related to charge transport, interfacial recombination, and ion migration—factors that significantly affect device stability and performance. Our study presents an advanced characterization approach combining J–V, Suns-V_{oc}, and impedance spectroscopy (IS) with multi-biasing analysis to disentangle the effects of mobile ions and energetic band offsets at perovskite/contact interfaces in inverted (p–i–n) architectures. By integrating experimental IS data with drift-diffusion (DD) simulations, we provide deeper physical insights into charge carrier dynamics, recombination mechanisms, and interfacial selectivity. Our findings reveal that high energetic band offsets at charge transport layers (CTLs) can limit the fill factor (FF) and open-circuit voltage (V_{OC}), while ionic accumulation modulates capacitive and recombination behavior. Understanding these complex interdependencies is crucial for overcoming efficiency bottlenecks and enhancing long-term PSC stability, paving the way for the optimization of next-generation tandem and scalable perovskite-based solar technologies.

[a]TotalEnergies OneTech, 91120 Palaiseau, France. E-mail: medina.juanpablo@outlook.es
[b]Institut Photovoltaïque d'Ile-de-France (IPVF), 18 Boulevard Thomas Gobert, 91120 Palaiseau, France. E-mail: pilar.lopez-varo@ipvf.fr
[c]Université Paris-Saclay, CentraleSupélec, CNRS, Laboratoire de Génie Electrique et Electronique de Paris, 91192 Gif-sur-Yvette, France
[d]Sorbonne Université, CNRS, Laboratoire de Génie Electrique et Electronique de Paris, 75252, Paris, France
[e]Department of Electronic, Electrical and Automatic Engineering, Universitat Rovira i Virgili, 43007 Tarragona, Spain
[f]Institut Photovoltaïque d'Île-de-France (IPVF), CNRS, Ecole Polytechnique - IP Paris, Chimie Paristech - PSL, UMR 9006, 18 Boulevard Thomas Gobert, Palaiseau 91120, France. E-mail: philip.schulz@cnrs.fr

Introduction

Perovskite solar cells (PSCs) are arguably the emerging photovoltaic (PV) technology of the decade, recently achieving certified power conversion efficiencies (PCEs) of 27.3% and 34.8% for single junction and silicon/perovskite tandem devices, respectively.[1] Their exceptional optoelectronic properties, including high absorption coefficients, long carrier diffusion lengths, defect tolerance, and tunable bandgap (E_g);[2] combined with low-temperature processability, make them strong

candidates for large scale industrialization.[2–4] However, their limited long-term stability remains a challenge.[5] A major factor underlying this instability is the presence of mobile ions within the perovskite absorber, whose redistribution under electrical bias and illumination modifies the internal electric field and affects charge-carrier dynamics.

Standard photovoltaic characterization methods, including current density–voltage (J–V) and Suns-V_{oc} measurements, are routinely employed to evaluate device performance and infer recombination mechanisms.[6–9] Their interpretation typically relies on the assumption of fast electronic charge-carrier response under steady-state conditions.[10,11] In PSCs, however, this assumption is frequently invalidated by slow ionic motion. The measured optoelectronic response reflects a convolution of electronic transport and recombination with bias-dependent effective built-in potentials (V_{bi}),[12] contact instabilities,[13–16] interfacial band offsets[7,17] and electric field screening due to mobile ion redistribution within the perovskite (PK) layer.[18–20] Among these, ionic accumulation at PK/charge transport layer (CTL) interfaces can dynamically reshape recombination pathways, impede charge extraction, and induce J–V hysteresis.[21] Consequently, the ideality factor derived from J–V or Suns-V_{oc} measurements alone provides limited insight into underlying losses. Decoupling these coupled electronic and ionic processes requires characterization techniques capable of resolving distinct temporal scales, supported by physical interpretation *via* drift-diffusion (DD) simulations.[22,23]

Impedance spectroscopy (IS) is a powerful method to probe these coupled dynamics in the frequency domain. PSCs exhibit characteristic impedance features spanning multiple decades in frequency, reflecting fast electronic processes in the PK bulk and slower ionic redistribution and interfacial charge accumulation.[24,25] The strong coupling between these processes produces complex spectra, including pronounced low-frequency capacitances and bias-dependent resistive elements. Multiple equivalent electric circuit models (ECMs) have been proposed to interpret these responses,[25–29] mainly depending on the given operating conditions such as voltage bias and light illumination under short-circuit (SC), maximum power point (MPP) or open-circuit (OC) conditions, as well as on device-specific factors including composition and degree of degradation. The use of general ECMs, for the interpretation of IS spectra in PSCs, remains limited. A unified physical understanding of IS in PSCs therefore requires models that incorporate coupled electronic and ionic transport across operating conditions.

Bias-dependent IS offers complementary insight into the dominant device physics. Under SC conditions, the impedance response primarily reflects charge transport and extraction processes.[30] Under OC conditions, the IS response is governed by recombination and diffusion-driven mobile ionic redistribution.[20,24,25] This is due to the device operating at zero current flow and near-flat-band conditions in the case of standard one sun illumination (open circuit voltage close to the V_{bi}). At the MPP, the high nonlinearity in the J–V response, together with the overlap of charge transport-recombination and extraction, complicates the interpretation of IS spectra. Although IS in PSCs has been widely studied under OC[31–33] and, more recently, under SC conditions,[30] a unified framework that consistently combines both regimes and enable direct comparison with DD simulations remains limited. In this context, a multi-bias approach is essential to resolve the coupled effects of electric field screening, recombination, and ionic dynamics, which is the focus of this study.

In this work, we present a comprehensive optoelectric characterization methodology for PSCs, combining J–V, Suns-V_{oc} and IS with a multi-biasing approach to quantitatively resolve coupled electronic–ionic effects in PSCs. Using an inverted (p–i–n) architecture as a case study, IS measurements are performed under SC and OC conditions over a wide range of illumination intensities. To enable a physically grounded interpretation, the experimental spectra are analyzed using ECMs and compared with the ECM fitting of the one-dimensional DD simulations performed with the open source *Driftfusion* code.[34] To the best of our knowledge, this work provides the first study integrating both OC and SC regimes through combined experimental and DD simulations. In particular, we analyze the IS data through the representation of resistive and capacitive elements as a function of short-circuit current density (J_{SC}) and open-circuit voltage (V_{OC}). First, DD simulations are used to evaluate the impact of key device parameters, with particular emphasis on mobile ion concentration, and to identify new correlations with high- and low-frequency resistive components. We analyze the effect of field screening and IS response difference between SC and OC conditions. Subsequently, the combined experimental–numerical framework enables extraction of key physical parameters, including carrier mobility (μ_{PK}), mobile ion concentration (N_{ion}), and shunt resistance (R_{SH}) from SC measurements. In addition, ideality factors (n_{id}) derived from dark J–V and Suns-V_{oc} analyses are compared with those obtained from OC impedance, establishing a consistent framework for assessing dominant recombination pathways. This approach further enables evaluation of the coupled effects of mobile ions and interfacial energy band offsets at perovskite/CTL interfaces.

Results and discussion

In this work, we analyzed PSCs with an inverted (p–i–n) configuration that were fabricated on FTO/glass substrates with the structure glass/FTO/NiO_x/perovskite/C_{60}/SnO_2/Au, as depicted in Fig. 1(a). First, dynamic light J–V curves were measured under 1 sun equivalent illumination and compared with DD simulations using the one-dimensional *Driftfusion* code (see the simulated device structure in Fig. 1(b)). For the device performance analysis, we focused on the variation of four key parameters in the PSCs. First, the carrier mobility in the perovskite μ_{PK} was varied from 0.2 to 20 $cm^2\ V^{-1}\ s^{-1}$, covering the typical range reported in the literature,[35] with electron and hole mobilities assumed to be equal for simplicity. Second, the mobile ion concentration N_{ion} was varied from 10^{15} cm^{-3} to 10^{19} cm^{-3} (ref. 36 and 37), considering two mobile ion species (cations and anions) present within the perovskite layer. From the J–V simulations, an ionic concentration close to 10^{18} cm^{-3} is expected considering the set of fixed device parameters

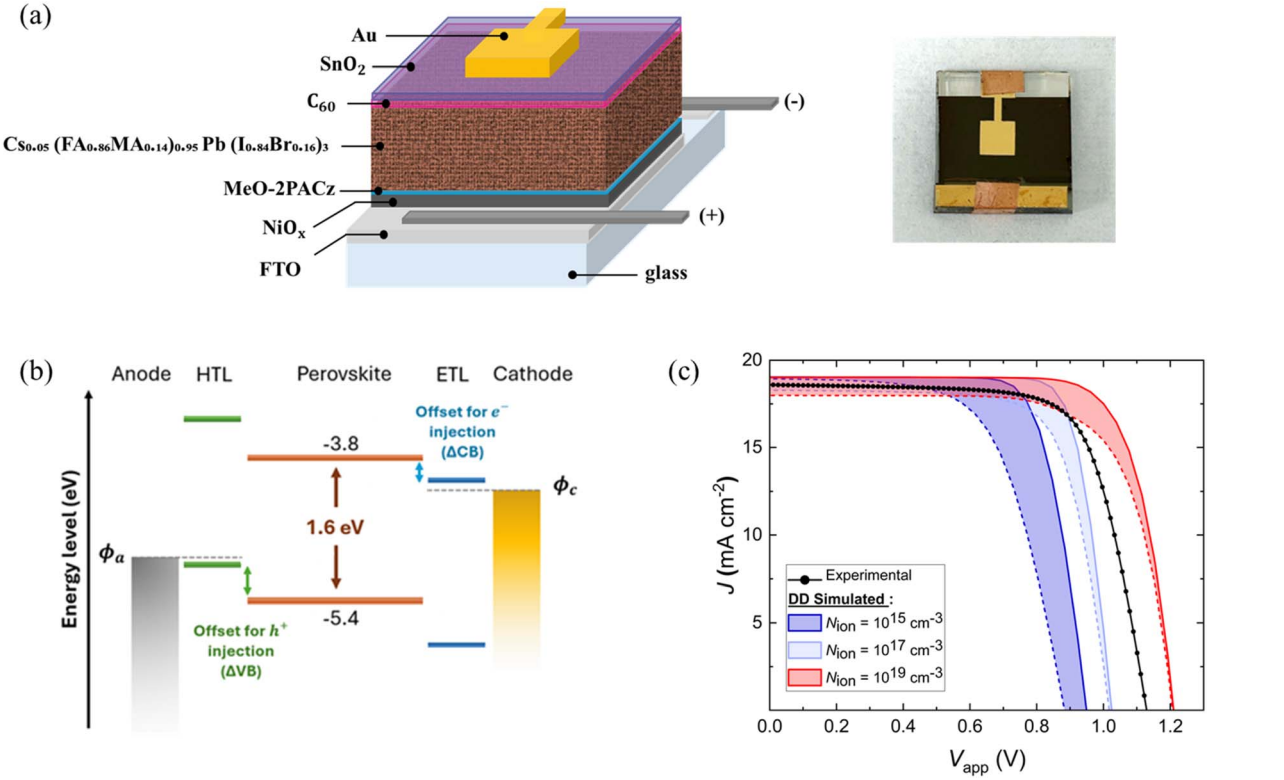

Fig. 1 (a) PSC schematic and corresponding top-view photograph deposited on FTO/glass. (b) Energy levels of the one-dimensional structure, before contact equilibrium, defined in DD simulations. (c) Experimental *vs.* DD simulated *J*–*V* curves, varying N_{ion} (cm^{-3}) = {10^{15}, 10^{17}, 10^{19}} and μ_{PK} ($cm^2\ V^{-1}\ s^{-1}$) = {0.2, 20}, at τ_{PK}^{SRH} = 1 μs and a low V_{bi} = 0.6 V (ΔV_B = 500 meV and ΔC_B = 300 meV). All *J*–*V* scans are simulated and experimentally performed in reverse direction at 30 mV s^{-1} and under 1 sun equivalent illumination.

(Fig. 1(c)). Further details regarding device fabrication, parameter selection (Table S1), and simulation methodology are provided in Section S1 of the SI. Third, the energy band offsets and built-in potential (V_{bi}) are defined as the difference between the anode and cathode work functions ϕ_a–ϕ_c (Fig. 1(b)). Interfacial band misalignment can effectively reduce V_{bi} impacting the *J*–*V* characteristics (see Fig. 3). In the simulations, V_{bi} is modified by varying the valence band offset ΔV_B at the perovskite/HTL interface and the conduction band offset ΔC_B at the perovskite/ETL interface through adjustment of the electron affinity of the respective CTLs. The CTLs are assumed to be highly doped, with their Fermi level positioned 100 meV from the band edge (conduction band for the ETL and valence band for the HTL, respectively). For simplicity, metal contacts are fixed as ohmic, and their Fermi level is perfectly aligned with the respective CTL Fermi level as an approximation in the DD model (SI section S1). Fourth, bulk recombination is modelled *via* defect-assisted Shockley–Read–Hall (SRH) processes assuming a single trap level[34] characterized by equal electron–hole lifetimes ($\tau_{PK}^{SRH} = \tau_e = \tau_h$) in the PK bulk.

After the *J*–*V* measurements, the IS response was measured under dark conditions and increasing illumination intensity (Ψ) from 10^{-4} to 1 sun (1000 Wm^{-2}), in the range of 100–1 MHz under ambient conditions and at a controlled temperature of 25 °C. Measurements were performed under both SC and OC conditions. The results are shown in Fig. 2, as Nyquist plots with real (Z') *vs.* ($-Z''$) imaginary semicircle representation and the corresponding frequency-dependent capacitance Bode plots.

Impedance spectra were fitted to the selected ECM, as shown in the inset of Fig. 2(d). The model consists of a nested configuration connected in line with a series resistance (R_S), accounting for contact- and transport-related ohmic losses. Two primary Voigt elements, each comprising a resistor (R) in parallel with a capacitive element (C), describe the high-frequency (HF) and low-frequency (LF) responses, with characteristic relaxation times $\tau = RC$. To account for non-ideal capacitive behaviors arising from interfacial inhomogeneities and material disorder, ideal capacitors were replaced by constant phase elements (CPEs), reflecting a distribution of relaxation times rather than a single one.[38] The high-frequency semicircle (ω > 1 kHz) is usually attributed to electronic transport-recombination and geometric capacitance effects of the multilayer device stack. A second semicircle at low frequencies (tens Hz to mHz) is ascribed to additional slow ionic–electronic dynamics and its coupling to interfacial charge accumulation and recombination.

The fitted values of the individual R and C elements were analyzed as a function of J_{SC} and V_{OC}. To interpret the experimental results, IS spectra were simulated using DD simulations under equivalent bias and illumination conditions, while varying key device parameters, particularly the mobile ion concentration. Under SC conditions and low illumination, the

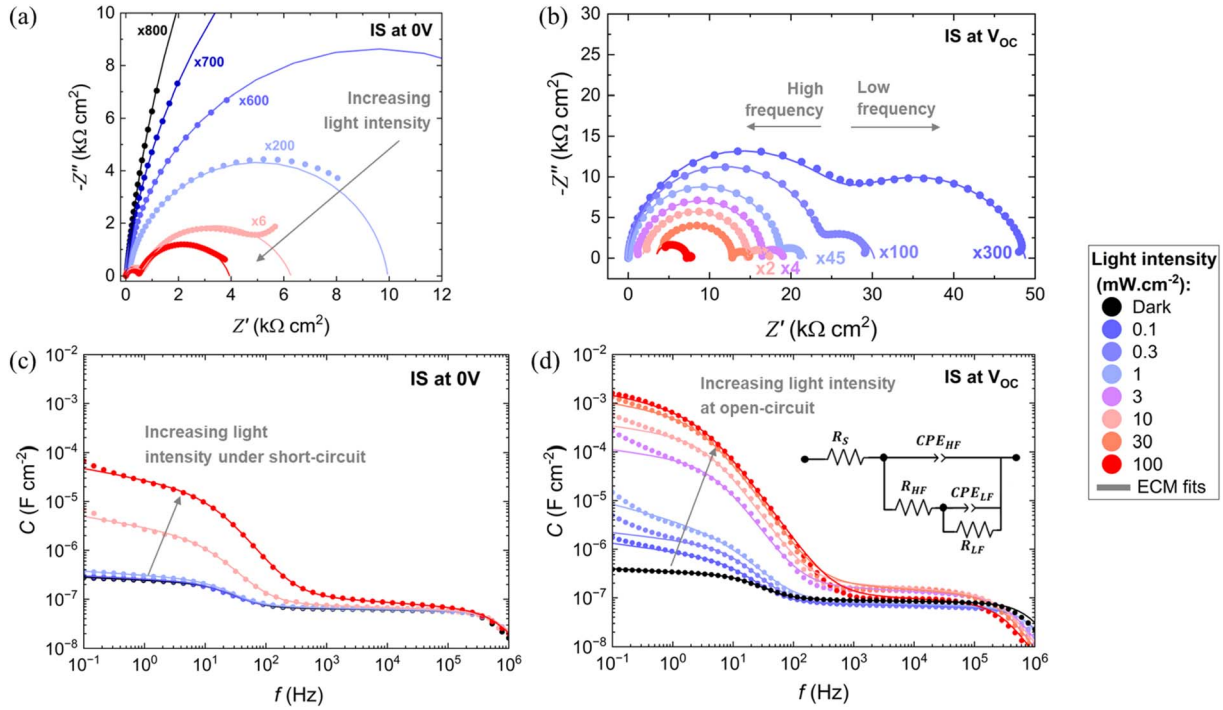

Fig. 2 IS data with increasing Ψ, measured under SC (a and c) and under OC (b and d) bias conditions, presented as: Nyquist plots (a and b), with real Z' *vs.* $-Z''$ imaginary components. Multipliers indicate the required scale-up factor for full magnitude display in measurements towards low Ψ conditions. Bode plots (c and d), with frequency-dependent capacitance. Experimental data (dots) and respective fits (solid lines) to the selected ECM, as the inset depicted in (d).

LF semicircle is often not fully closed within the frequency range measured experimentally (until 100 mHz), which may introduce uncertainty in the extraction of the LF components (R_{LF} and C_{LF}). Therefore, experimental accuracy is very important when analyzing extrapolated LF parameters. DD simulations were extended to lower frequencies (down to 0.1–1 mHz), enabling a more reliable estimation (see SI Section S4 and Fig. S4.17). However, when comparing simulations and experiments, uncertainties related to extrapolation and parameter correlation should be considered. Both experimental and simulated spectra were fitted using the same ECM, enabling a consistent extraction of circuital elements, and a summary of the fitting parameters, including errors, is provided in the SI (Section S4, Tables S4.1–S4.4).

A shunt resistance R_{SH} was not explicitly included in the selected ECM, although it is included in the DD simulator. The contribution of R_{SH} to the resistive components (R_{HF} and R_{LF}), which depends on bias and illumination conditions,[25] is analyzed in the next sections. Further details on the measurement protocol, the impedance transfer function of the selected ECM (with and without the R_{SH} element), and discussion of additional RC contributions reported for PSCs are provided in Section S2 of the SI.

Analysis of *J*–*V* and Suns-V_{oc} characterization

Performance parameters extracted from *J*–*V* measurements under 1 sun illumination are shown in Fig. 3 and summarized in Table S3.1 of the SI. Experimental results (dot distributions) are compared with DD simulations (plots). Although V_{OC} values exceeding 1100 mV were achieved, reduced J_{SC} and FF limited the PCE compared with state-of-the-art inverted PSCs[39] (Table S3.2 of the SI). While FF losses are partly attributable to high series resistance (R_s) and/or low shunt resistance (R_{SH}), reduced J_{SC} may arise from optical or extraction losses.[40] DD simulations performed with fixed R_s, R_{SH}, and photogeneration show that the performance limitations also originate from coupled effects of reduced carrier mobility and increased mobile N_{ion}, which appears to be governed by band offsets, captured *via* variations in V_{bi}.

Energy band offsets greater than 300 meV (low V_{bi}) are detrimental for the PCE, V_{OC} and FF in PSCs.[13,14,40] However, simulations (Fig. 3(a–c)) reveal enhanced tolerance to such band offsets as N_{ion} increases from 10^{15} to 10^{19} cm^{-3}, due to ionic screening that lowers interfacial barriers even under forward bias (MPP and OC; SI Section S4, Fig. S4.1 and S4.2), in line with previous reports.[19,20] Yet, as shown in Fig. 3(d), at low μ_{PK}, high N_{ion} hinders charge extraction and reduces the J_{sc},[40] evidencing a trade-off between barrier screening and transport constraint. We note that for other device configurations with low doped CTLs and high interface recombination, an increase of the mobile ion concentration leads to a decrease of the PCE.

Experimental dark *J*–*V* curves and Suns-V_{oc} (J_{sc}–V_{OC} points) measurements are presented in Fig. 4(a). Dark *J*–*V* exhibit three regimes: shunt-dominated leakage at low bias (V < 0.6 V), a recombination-controlled intermediate region, and R_S-limited saturation at high bias (V > 1.1 V), when V_{bi} is surpassed and the

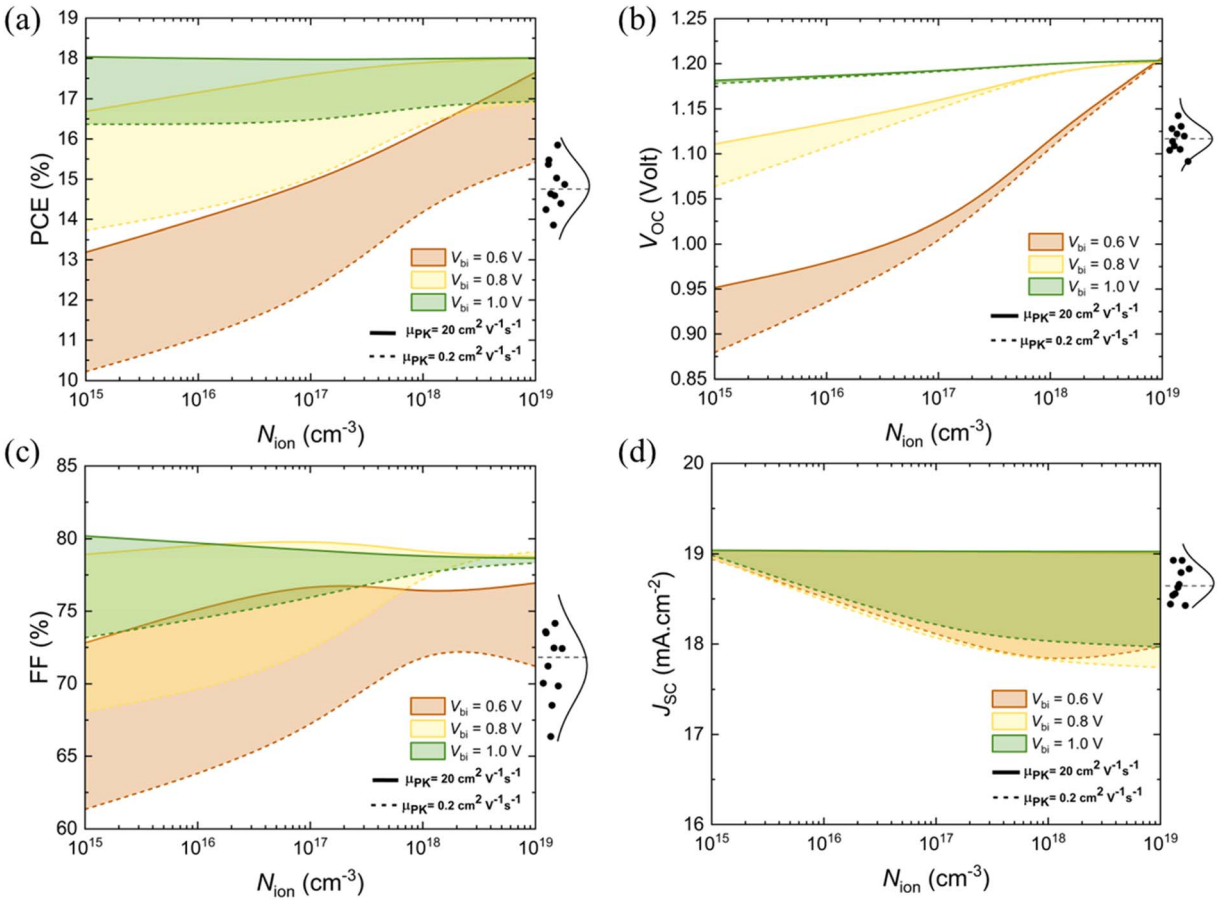

Fig. 3 Simulated power conversion efficiency (PCE) (a), open-circuit voltage (V_{OC}) (b), fill factor (FF) (c) and short-circuit current (J_{SC}) (d), extracted from DD simulated J–V curves assuming $\tau_{PK}^{SRH} = 1$ μs and varying V_{bi} (V) = {0.6, 0.8, 1}, within the ranges of high (solid lines) and low (dashed lines) electron–hole mobility μ_{PK}. Side comparison with experimental results (black dots) with dashed horizontal lines indicating the median of the measured distributions.

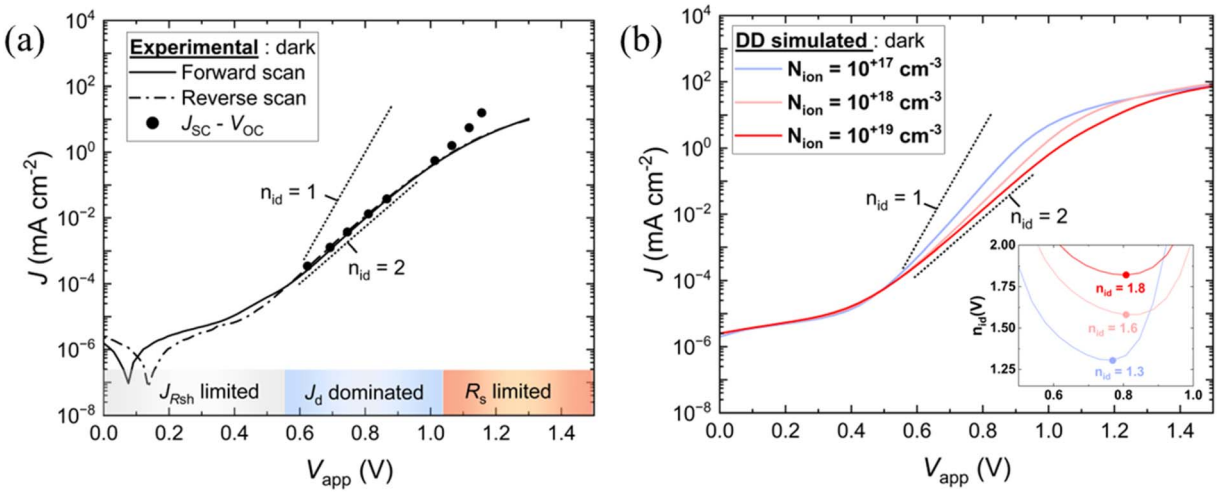

Fig. 4 (a) Dark J–V curves in forward (solid) and reverse (dashed) sweep directions at 30 mV s^{-1}, directly compared with Suns-V_{oc} (J_{sc}–V_{OC}) measurements (solid dots) for recombination analysis at the diode-like current (J_d) zone. (b) DD simulated dark J–V curves (reverse scans), varying N_{ion} (cm^{-3}) = {10^{17}, 10^{18}, 10^{19}, at $\mu_{PK} = 0.2$ cm^2 V^{-1} s^{-1}, low V_{bi} at 0.6 V ($\Delta V_B = 500$ meV and $\Delta C_B = 300$ meV) and $R_{SH} = 10^8$ Ω cm^2. The n_{id} values of 1 and 2 were estimated using linear regression fits to eqn (1) and from its local derivative minimum applied to the J–V (n_{id} (V) inset in (b)).

injection of charge is significative. In the recombination regime, the current density (J_d) follows the diode expression:[41]

$$J_d(V) = J_o\left(\exp\left[\frac{qV_{int}}{n_{id}k_BT}\right] - 1\right) \quad (1)$$

where k_B is the Boltzmann constant, q is the elementary charge, J_0 is the saturation current density pre-factor, n_{id} is the ideality factor and T is the temperature of the internal diode. The R_s induces $V = V_{int} - J\,R_S$, and the internal voltage, V_{int}, approximates the quasi-Fermi level splitting ($\Delta E_F/q$).[11,42,43] Therefore, Suns-V_{oc} measurements directly probe intrinsic recombination, as $V_{OC} = V_{int}$ under OC conditions and a sufficiently large R_{SH} [8,9] Experimental J_{sc}–V_{OC} points in Fig. 4(a) closely reproduce the J_d profile without the R_s saturation effect towards high applied voltages.

An ideality factor n_{id} close to 2 (see SI, Tables S3.3 and S3.4) was obtained experimentally using eqn (1), as shown in Fig. 4(a), which suggests dominant SRH recombination.[8,41,44] In classic recombination theory for p–n junctions, $n_{id} = 1$ indicates that the J–V response is dominated by band-to-band recombination in the quasi-neutral regions, while $n_{id} = 2$ corresponds to dominant SRH recombination mediated by deep defects in the space charge region. In inverted PSCs, strong interfacial recombination may reduce the apparent n_{id} towards unity.[7,17] Within the DD framework, modifications of V_{bi}, *via* ΔCB (PK/ETL), ΔV_B (PK/HTL), or interfacial N_{ion} accumulation, directly modulate carrier collection and modify the magnitudes of n_{id} and J_0.[12] As shown in Fig. 4(b) the diode-regime recombination analysis is highly dependent on N_{ion}, complicating quantitative extraction of n_{id} in these devices.

Comparable n_{id} values were obtained from Suns-V_{oc} and dark J–V curves (SI, Tables S3.3 and S3.4), whether extracted by linear regression or from the local derivative yielding the minimum $n_{id}(V)$, as shown in the inset of Fig. 4(b). As Suns-V_{oc} measurements largely eliminate R_S and R_{SH} contributions, recombination remains governed by minority carrier concentrations. Under illumination, high N_{ion} can therefore produce apparent n_{id} equal and above 2 (SI, Fig. S4.3).

Consistent with the J–V analysis, at a low μ_{PK} and high band offsets, the tolerance effect at high N_{ion} cannot fully compensate recombination losses. Simulations show electron–hole concentration imbalances within the PK layer (see SI, Fig. S4.4) for large band offsets ΔV_B and ΔC_B at the PK/HTL and PK/ETL interface, respectively. These coupled interactions between band offsets and mobile ions, and their impact on recombination, are further examined through the comparison between experimental and simulated IS in the following sections.

IS under short-circuit conditions at variable illumination

To further interpret the device behavior, R_{HF} and R_{LF} are plotted as a function of J_{sc} in double-logarithmic representation, as shown in Fig. 5, comparing experimental data with DD simulations varying μ_{PK} and N_{ion}. Under SC conditions, the internal electric field, determined by V_{bi}, can be partially screened by mobile ion accumulation at the PK/CTL interfaces. However, varying V_{bi} from 0.6 to 1.0 V in the simulations does not produce significant changes in the resistive or capacitive response across

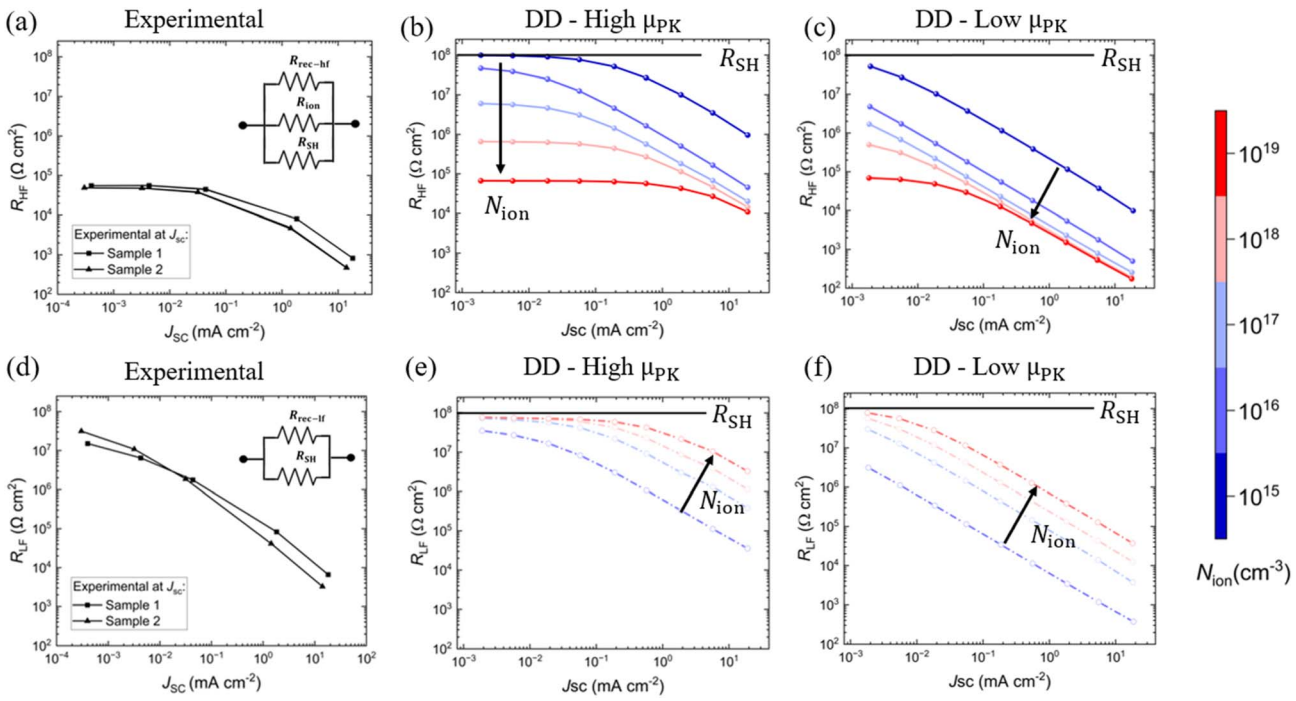

Fig. 5 R_{HF} (a–c) and R_{LF} (d–f), as a function of J_{SC} under increasing Ψ from 1×10^{-4} to 1 sun equivalent, extracted from IS fits to the selected ECM (as the inset of Fig. 4(d)). For DD simulations, the ion concentration varies in the range of $N_{ion} = [10^{15} - 10^{19}]$ cm^{-3}, with $V_{bi} = 0.6$ V, $R_{SH} = 10^8\ \Omega\ cm^2$ and $\tau_{PK}^{SRH} = 1\ \mu s$. Effect of increasing N_{ion} at high (b and e) *vs.* low (c and f) electronic mobility, μ_{PK} (cm^2 V^{-1} s^{-1}) = {0.2, 20}, respectively.

the explored ranges of N_{ion} and τ_{PK}^{SRH}. Noticeable deviations arise at low V_{bi} under transport-limited conditions (*i.e.* at lower μ_{PK}) in the PK, as detailed in SI Fig. S4.5.

In general, R_{HF} and R_{LF} exhibit two distinct regimes as a function of J_{sc}. At low Ψ, both resistances exhibit an apparent plateau reaching a maximum value, denoted here as R'_{SH}. At higher Ψ, they decrease linearly with increasing J_{sc}, consistent with a dominant recombination resistance (R_{rec}) associated with the enhanced photogenerated carrier density in the PK bulk. Accordingly, despite their different frequency origins (HF and LF), each resistance contribution can be independently described by a parallel combination of an effective R'_{SH} and an illumination intensity-dependent $R_{rec}(J_{sc})$, expressed as follows:

$$R_{HF} = \frac{R'_{SH-HF} \times R_{rec-HF}(J_{sc})}{R'_{SH-HF} + R_{rec-HF}(J_{sc})} \quad (2)$$

$$R_{LF} = \frac{R'_{SH-LF} \times R_{rec-LF}(J_{sc})}{R'_{SH-LF} + R_{rec-LF}(J_{sc})} \quad (3)$$

Focusing on the R'_{SH-HF} plateaus in Fig. 5(a–c), we find that R_{HF} is affected by an additional resistive contribution (R_{ion}) coming from the static N_{ion} distribution, which screens the internal electric field and remains effectively invariant within the HF perturbation range. The effect of mobile ions in the HF response has been often considered negligible in previous studies.[24–26,28] For the PSC architecture investigated here, the combined IS and DD analysis suggests N_{ion} in the range of 10^{18}–10^{19} cm^{-3}. In the case of low mobile ion concentration and ideally no shunt resistance, the plateau would originate from a resistive dark recombination that is in parallel with R_{ion}. This resistance R_{ion} is independent of illumination intensity and should be distinguished from the R_{rec-LF}, which is rather associated with additional modulation of recombination from slow ion motion in the LF range.

DD simulations also show that the slope of the linear R_{rec} decay, both at HF Fig. 5(b and c) and LF in Fig. 5(e and f), is independent of the selected parameters. Additional simulated IS results (SI, Fig S4.6) explore $\mu_{PK} = [0.2–20]$ cm^2 V^{-1} s^{-1} and τ_{PK}^{SRH} from 10 ns to 1 μs, spanning typical recombination rates reported for comparable PSC devices.[20,30,45] The illumination range in which R_{rec} predominates is strongly governed by μ_{PK} and τ_{PK}^{SRH} in the PK layer. Hence, we find that the best agreement with experimental IS fits is obtained for medium-to-low mobilities of $\mu_{PK} = [0.2–2]$ cm^2 V^{-1} s^{-1} and $\tau_{PK}^{SRH} = 1$ μs. A complementary analysis of IS fits, that takes into account the impact of the imbalance of the electron–hole mobilities (μ_e/μ_h) in the PK, can be found in the SI (see section S4, Fig. S4.16). Notably, the same R–J_{sc} profiles are obtained in DD simulations when varying μ_{PK} and τ_{PK}^{SRH} independently, as long as their product $\mu_{PK} \cdot \tau_{PK}^{SRH}$, which determines the diffusion length $L_D = \sqrt{D\tau}$, remains constant for a given N_{ion}. This behavior arises from the implementation of the Einstein relation in the DD simulations, which couples mobility and diffusion coefficient. Under dark conditions, where current is dominated by shunt-assisted leakage recombination, both R'_{SH-HF} and R'_{SH-HF} would be expected to converge toward R_{SH}, consistent with the J–V analysis. Experimentally, R_{HF} and R_{LF} exhibit markedly different magnitudes at the lowest illumination ($\Psi = 10^{-4}$ sun), as shown in Fig. 5(a) and (d). DD simulations at high μ_{PK}, in Fig. 5(b) and (e), indicate that R_{LF} approaches the input $R_{SH} = 10^8$ Ω cm^2 across all N_{ion}; whereas R_{HF} progressively departs from R_{SH} with increasing N_{ion}. The pronounced divergence between R_{HF} and R_{LF} near dark conditions at 0 V bias suggests that the HF and LF responses are differently influenced by R_{SH}, mediated by ionic effects in the PK layer, as illustrated by the ECMs in Fig. 6(a) and (b). From the maximum experimental R_{LF} values, the dark R_{SH} is estimated to be equal or higher than 10 MΩ cm^{-2} (lower R_{SH} effects on simulated IS are shown in SI Fig. S4.7).

It should be noted that the alternative ECMs proposed in Fig. 6(a and b) are not intended for a direct experimental implementation, as parallel resistive elements are reduced to a single equivalent resistance in the fitting process. Rather, they serve as a conceptual framework to illustrate the distinct physical contributions inherent to the R_{HF} and R_{LF} components arising from the multiple "aggregated" ionic and electronic effects identified through DD simulations.

For R_{LF}, shown in Fig. 5(d–f), increasing N_{ion} does not impact the R'_{SH-LF} plateau, but enhances R_{rec-LF} at high illumination. DD simulations indicate that internal bulk screening in the perovskite is reached for $N_{ion} \sim 10^{17}$ cm^{-3} (see SI, Fig. S4.2)

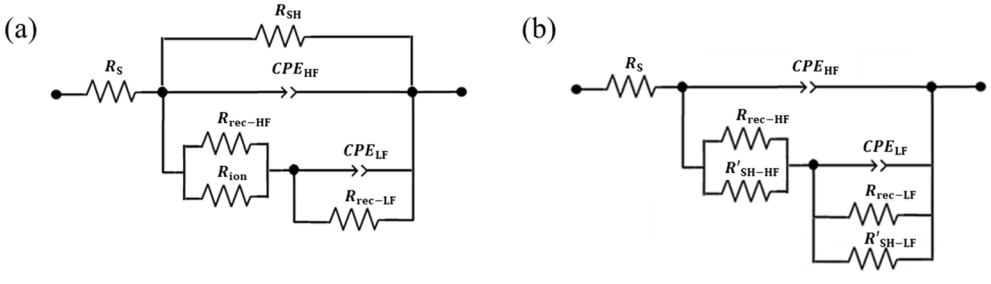

Fig. 6 (a) Extended ECM proposed from the IS analysis of inverted PSCs in this study. It includes resistance dependence on the static N_{ion} distribution (R_{ion}) at high frequencies, in parallel with internal diode recombination (R_{rec-HF}) and parasitic R_{SH}. At low frequencies, the diode recombination (R_{rec-LF}) is modulated by mobile ions in the PK. (b) Equivalent structure from the perspective of individual shunt effects at high (R'_{SH-HF}) and low (R'_{SH-LF}) frequencies, resulting from a dynamic role of N_{ion} in the parasitic leakage currents, respectively.

enabling ion redistribution under small LF perturbations. Consequently, the interfacial ion layer that contributes an additional R_{ion} at HF becomes less effective at LF due to ion migration. This is of particular importance because, for all the IS fits in this study, the magnitude of R_{LF} was always higher than that of R_{HF}, indicating that the LF contribution dominates the resistive component of the J–V response at J_{SC}. Similar trends have been reported in DD simulations of inverted PSCs, where $N_{ion} > 10^{17}$ cm^{-3} leads to an overall resistance increase (primarily dominated by R_{LF}) and a concurrent reduction in the low frequency capacitance.[30] Importantly, as shown in Fig. 5, R_{LF} and R_{HF} exhibit opposite dependences on mobile ion concentration. An increase in N_{ion} reduces the HF resistance due to enhanced internal field screening, while it increases the LF resistance by modulating charge accumulation at the interfacial barriers. Complementary C–J_{sc} profiles are included in the SI (see Fig. S4.8).

Within the wide range of parameters explored in our simulations, the high frequency SC resistance in the dark and under illumination shows a clear dependency on the recombination parameters and the mobile ion concentration, given a sufficiently high shunt resistance. This suggest that, depending on the nature of the coupled capacitance, the high frequency RC response time τ_{HF} can be considered as a recombination lifetime. However, our analysis also indicates that the low frequency resistance under dark and low illumination SC conditions is governed by the shunt resistance and shows no dependency on the concentration of mobile ions or the recombination parameters (except for high recombination rates). This implies that the RC response time τ_{LF} associated with the corresponding dark low frequency process cannot be straightforwardly interpreted as a recombination lifetime. Furthermore, this also questions the nature of τ_{LF} under illumination, whose values typically are in the order of the dark τ_{LF}. These findings are not only important for our general understanding of the recombination-related features of impedance spectra in PSCs, but they are particularly relevant for perovskite-based indoor photovoltaic and photodetector applications.

IS under open-circuit conditions at variable illumination

The combined protocol of IS measurements under OC conditions, compared with DD-simulations, enables a refined recombination analysis by separating fast HF processes, where ionic profiles remain effectively frozen, from slower LF dynamics governed by ion redistribution. We measured IS under open-circuit conditions ($V_{app} = V_{OC}$) increasing Ψ from 10^{-4} up to 1 sun illumination, which corresponds to $V_{oc} \approx 0.6$–1.2 V, as presented in Fig. 2(b) and (d). Lower voltages ($V_{OC} \leq 0.6$ V) were not accessible due to instrumental limitations. At very low Ψ, the OC response is expected to show trends similar to those reported under SC conditions due to the reduction of electron and hole carrier concentrations in the PK bulk.

The resulting R–V_{OC} plots present two regimes, analogously to the SC case, and are described using eqn (2) and (3). R_{HF} – V_{OC} profiles are presented in Fig. 7(a–c) (R_{LF} – V_{OC} profiles are included in SI section S4, Fig. S4.12) for which the experimental IS data were fitted with DD simulations. We particularly

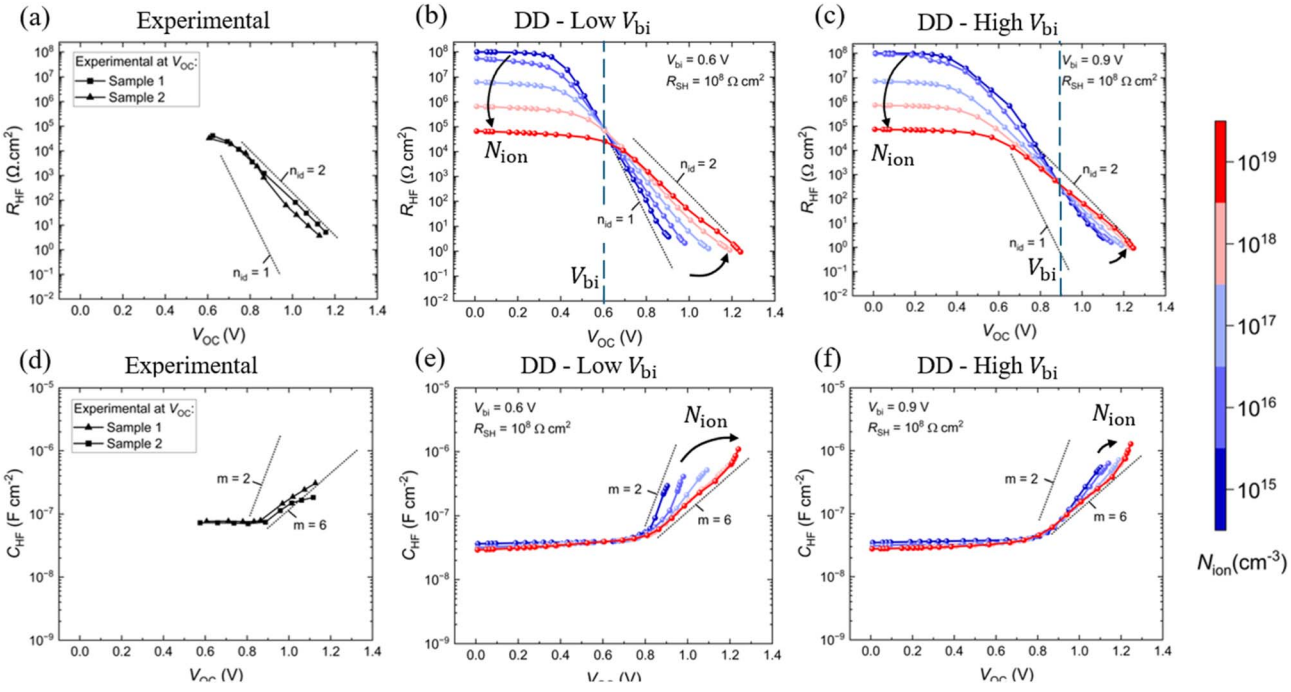

Fig. 7 R_{HF} (a–c) and C_{HF} (d–f) under open-circuit conditions for different illumination intensities from 10^{-4} up to 1 sun equivalent, obtained from IS fits to the selected ECM (inset in Fig. 2(d)). Comparison of experimental IS measurements in (a) and (d) *versus* DD simulations in (b and c) and (e and f) varying N_{ion} and V_{bi} at $\tau_{PK}^{SRH} = 1$ µs. The n_{id} and m reference values, indicated by dashed lines, were determined using eqn (4) and (5), respectively.

highlight the impact of energy band offsets at the PK/HTL interface (ΔV_B, in Fig. 1(b)), which modify V_{bi}, and of the mobile ion concentration on the IS response under OC conditions.

At low V_{OC} < 0.6 V, R_{HF} displays a plateau R'_{SH-HF} consistent with a high R_{SH} ($\sim 10^8$ Ω cm^2), whose magnitude is modulated by N_{ion} (see the effect of low R_{SH} under varying N_{ion}, in SI, Fig. S4.13). At higher V_{OC}, once R_S and R_{SH} contributions are excluded and in the absence of strong injection/extraction barriers (resulting in a strong deviation of V_{int} from V_{app}),[46] R_{HF} is predominantly governed by diode recombination under flat-band conditions, following the characteristic exponential decay of R_{rec}:[8]

$$R_{rec} = \frac{n_{id}\, k_B T}{q J_o} \exp\left[-\frac{q\ V_{OC}}{n_{id}\ k_B T} \right] \quad (4)$$

In line with the approach of Caprioglio *et al.*,[7,17] we evaluated the impact of ΔV_B on the recombination analysis by extracting n_{id} from the R_{HF}–V_{OC} slope (eqn (4)). Simulated IS fits were compared for moderate band offsets ($\Delta V_B = \Delta C_B$ of 250 meV) and high band offsets (ΔV_B of 500 meV and ΔC_B of 300 meV) mainly at the PK/HTL interface. The corresponding cases, with V_{bi} = 0.9 V and 0.6 V, are shown in Fig. 7(b) and (c), respectively.

Comparing experimental data (Fig. 7(a)) with DD simulations (Fig. 7(b and c)) in the R_{rec-HF} decay regime at increasing V_{oc} reveals that higher N_{ion} leads to larger extracted n_{id} values, consistent with the dark *J*–*V* analysis. Experimental n_{id} (HF) values closer to 2 for representative devices confirm SRH-dominated recombination in the investigated PSCs. At the high N_{ion} range (10^{18}–10^{19} cm^{-3}) identified under SC conditions, the electric field in the PK bulk becomes fully screened. Notably, at medium V_{bi} and high N_{ion}, the inflection point of R_{HF}–V_{OC} is at V_{bi}.

In PSCs, the resistance extracted from IS under OC conditions is commonly interpreted as electronic at HF, where ionic motion is effectively frozen, and as ion-modulated at LF due to ionic redistribution. The electronic resistance exclusively refers to the charge carriers (electrons and holes) that can follow the HF perturbation. In that sense, under OC conditions,[31] the HF response is governed by recombination consistent with diode behavior. However, even at HF, the resistance can be affected by the effect of mobile ions *via* field screening and modification of the charge density profile (as seen in Fig. 7). Our results show that this "ionic–electronic contribution separation" is most valid at V_{oc} near flat-band conditions (Fig. 7(b) and (c), dashed line), while deviations arise at lower illumination or away from V_{bi}. This approximation remains valid over a broader range of V_{app} approaching to $V_{bi,}$ particularly in devices with higher V_{bi} (Fig. 7(b and c)). Under OC conditions, LF features arise from ion-induced modulation of the internal electric field (linked to V_{bi}, see Fig. S4.12) and interfacial charge accumulation. Notably, devices with larger V_{bi} exhibit a reduced dependence of R_{LF} on the mobile ion concentration. By contrast, under SC conditions, both HF and LF resistive components are influenced by mobile ions through distinct mechanisms. Under low illumination conditions, the formation of a HF resistance plateau depends on the mobile ion concentration (if the electronic mobility is high enough), highlighting the impact of ionic screening on the nominally "electronic" response. At LF, R_{LF} is governed by interfacial charge accumulation and dependent on mobile ionic parameters. Therefore, mobile ions influence both HF and LF resistances, emphasizing the need for a unified ionic–electronic interpretation of IS spectra.

Experimental and simulated C_{HF}–V_{OC} profiles are shown in Fig. 7(d–f). In all cases, C_{HF} exhibits a bias-independent contribution up to 0.9 V, corresponding to the total geometrical capacitance (C^T_{geo}), followed by a pronounced increase (≈2–5 times within ~200 mV), whose magnitude depends on V_{bi} and N_{ion}. Illustratively, a second sample also showed an apparent saturation at high values of V_{OC} > 1.0 V (Fig. 7(d)). The monotonic increase is consistent with the onset of chemical-like electronic capacitance associated with carrier accumulation, whereas the saturation behavior may indicate additional parasitic contributions, such as contact depletion capacitance.[36,37,47] However, additional effects from a temperature rise in the device during IS measurements at high Ψ cannot be fully excluded. As a first approximation, C_{HF} increases exponentially towards higher V_{OC} following the relation:

$$C_{HF}(V) = C_0 \exp\left(\frac{qV}{m\ k_B\ T} \right) \quad (5)$$

where C_0 corresponds to the chemical capacitance at dark equilibrium and m to the factor limiting the voltage-dependent activation related to electron and hole accumulation in the PK layer at a given forward bias.[48] The effective C_{HF} values presented in Fig. 7(d–f) were calculated following the fitting methodology presented in section S2 of the SI (eqn (S23)). A summary of the IS fitting results is provided in section S4 of the SI (Tables S4.1–S4.4). At HF, the CPE_{HF} fits generally present values of α_{HF} > 0.91, indicating a response close to an ideal capacitance behavior, with limited impact on the extracted C_{HF} and m_{HF} values.

From DD simulations in Fig. 7(e and f), we observe that the defined ΔV_B offset shifts the activation of C_{HF} (V) towards higher V_{OC}, likely by changing the activation factor m, as in eqn (5). For large ΔV_B (*i.e.*, low V_{bi}) at low N_{ion}, the misalignment of the energy level at the PK/HTL interfaces increases the hole injection barrier under high V_{OC}, leading to electron accumulation in the PK bulk (see SI, Fig. S4.4).[49] Increasing N_{ion} effectively reduces this injection barrier due to ionic screening in the PK (see SI, Fig. S4.12). The saturation of C_{HF} at high V_{OC} is also reproduced in DD simulations, particularly for the case of large energy band offsets (Fig. 7(e)). Experimental extracted m values closer to 5 (Fig. 7(d)) suggest a high N_{ion} in the investigated PSCs. Although the parameter m can provide insight into the magnitude of N_{ion}, large extracted m values in an exponential fit may indicate that the capacitance–voltage dependence is not purely exponential, but instead associated with a transition between regimes and/or the overlap with polynomial or fractional space-charge capacitance contributions.

In this work, we do not include the analysis of additional inductive effects on performance loss, as reported in the IS literature for some PSCs. For all the IS fits presented, as shown

in Fig. 2, CPE values at HF and LF for the selected ECM displayed a dominant capacitive nature. However, we do observe some incipient inductive signatures only towards limiting frequencies <1 Hz for some experimental measurements under OC conditions at high illumination close to 1 sun. From DD simulations, we note that dominant inductive features, from mid to low frequencies (see SI Section S4, Fig. S4.10), can emerge mainly under conditions where $V_{OC} \approx V_{bi}$, as reported in literature.[32,50] The inductive behavior is generally associated with surface polarization and interfacial barriers that dynamically modulate charge injection and extraction under ion redistribution,[51,52] resulting in a phase delay between voltage and recombination currents.[51,53,54]

Conclusion

By combining *J*–*V*, Suns-V_{oc}, and multi-bias IS with drift-diffusion simulations, we conclude that the interplay between mobile ions and interfacial energy band offsets at perovskite/CTL interfaces can limit the electronic transport and recombination in inverted (p–i–n) PSCs, ultimately affecting the device performance. Pronounced band offsets at the PK/CTL interfaces were identified as a key factor limiting FF and V_{OC}. Dark *J*–*V* and Suns-V_{oc} analyses indicate high mobile ion concentrations ($N_{ion} = 10^{18}$–10^{19} cm^{-3}), which enhance tolerance to interfacial band offsets and influence the extracted n_{id}. However, high N_{ion} values cannot fully compensate for reduced charge transport in the case of low carrier mobility in the perovskite ($\mu_{PK} \sim 0.2$ cm^2 V^{-1} s^{-1}).

IS measurements under both SC and OC conditions combined with DD simulations were performed under equivalent bias and illumination, enabling a consistent interpretation of the impedance response. Experimental and simulated IS spectra were fitted with a common ECM as a function of J_{sc} and V_{oc}. IS under SC conditions enabled an independent estimation of the electronic mobility (0.2–2 cm^2 V^{-1} s^{-1}), mobile ion concentration (10^{18} – 10^{19} cm^{-3}), and the dark shunt resistance (10^7–10^8 Ω cm^2). Complementary OC at IS revealed distinct signatures of coupled ionic–electronic processes, linking resistive and capacitive responses to ion density and effective built-in voltage.

The role of the mobile ion concentration was analyzed for both regimes, SC and OC. Under SC conditions, the high- and low-frequency resistances exhibit distinct dependencies on ion concentration, associated with ionic screening and interfacial charge accumulation, respectively, highlighting their different physical origins. Under OC conditions, the analysis reveals that the high-frequency response approaches a purely electronic recombination regime near flat-band conditions influenced by the static ionic distribution, while low-frequency features reflect ion-modulated recombination. Our simulations yield that the extracted ideality factor is also affected by the effective built-in voltage. Finally, we show that under dark conditions at 0 V, the R_{LF} resistance is dominated by the shunt resistance and is largely independent of recombination and N_{ion}. Consequently, the associated R_C time constant cannot be directly interpreted as a recombination lifetime.

Overall, this integrated methodology provides a physically grounded framework to disentangle transport, recombination, and ionic effects in perovskite photovoltaics, offering guidance for interface optimization and device performance analysis.

Conflicts of interest

There are no conflicts to declare.

Data availability

The data supporting the findings of this study, including experimental measurements and device characterization data, are available within the article and its supplementary information (SI). Additional raw data generated during the study are available from the corresponding authors upon reasonable request. Supplementary information is available. See DOI: https://doi.org/10.1039/d6el00034g.

Acknowledgements

This work was supported by the French National Research Agency (Agence Nationale de la Recherche, ANR; Grant Nos. ANR-21-CE05-0022 and ANR-IEED-002-01) and by the National Association for Research and Technology (Association Nationale de la Recherche et de la Technologie, ANRT; Grant No. 2021/1814). The authors gratefully acknowledge this financial support.

References

1 M. A. Green, E. D. Dunlop, M. Yoshita, N. Kopidakis, K. Bothe, G. Siefer, X. Hao and J. Y. Jiang, Solar Cell Efficiency Tables (Version 66), *Prog. Photovolt.*, 2025, **33**(7), 795–810.
2 M. A. Green, A. Ho-Baillie and H. J. Snaith, The emergence of perovskite solar cells, *Nat. Photonics*, 2014, **8**(7), 506–514.
3 Y. Rakita, I. Lubomirsky and D. Cahen, When defects become 'dynamic': halide perovskites: a new window on materials?, *Mater. Horiz.*, 2019, **6**(7), 1297–1305.
4 S. Mazumdar, Y. Zhao and X. Zhang, Stability of Perovskite Solar Cells: Degradation Mechanisms and Remedies, *Front. Electron. Mater*, 2021, **2**, 712785.
5 D. M. Atia, A. A. Hassan, H. T. El-Madany, A. Y. Eliwa and M. B. Zahran, Degradation and energy performance evaluation of mono-crystalline photovoltaic modules in Egypt, *Sci. Rep.*, 2023, **13**(1), 13066.
6 S. J. Robinson, A. G. Aberle and M. A. Green, Departures from the principle of superposition in silicon solar cells, *J. Appl. Phys.*, 1994, **76**(12), 7920–7930.
7 P. Caprioglio, C. M. Wolff, O. J. Sandberg, A. Armin, B. Rech, S. Albrecht, D. Neher and M. Stolterfoht, On the Origin of the Ideality Factor in Perovskite Solar Cells, *Adv. Energy Mater.*, 2020, **10**(27), 2000502.
8 O. Almora, K. T. Cho, S. Aghazada, I. Zimmermann, G. J. Matt, C. J. Brabec, M. K. Nazeeruddin and G. Garcia-Belmonte, Discerning recombination mechanisms and

ideality factors through impedance analysis of high-efficiency perovskite solar cells, *Nano Energy*, 2018, **48**, 63–72.

9 P. Calado, D. Burkitt, J. Yao, J. Troughton, T. M. Watson, M. J. Carnie, A. M. Telford, B. C. O'Regan, J. Nelson and P. R. F. Barnes, Identifying Dominant Recombination Mechanisms in Perovskite Solar Cells by Measuring the Transient Ideality Factor, *Phys. Rev. Appl.*, 2019, **11**(4), 044005.

10 J.-F. Guillemoles, T. Kirchartz, D. Cahen and U. Rau, Guide for the perplexed to the Shockley–Queisser model for solar cells, *Nat. Photonics*, 2019, **13**(8), 501–505.

11 U. Würfel, D. Neher, A. Spies and S. Albrecht, Impact of charge transport on current–voltage characteristics and power-conversion efficiency of organic solar cells, *Nat. Commun.*, 2015, **6**(1), 6951.

12 U. Rau and T. Kirchartz, Charge Carrier Collection and Contact Selectivity in Solar Cells, *Adv. Mater. Interfaces*, 2019, **6**(20), 1900252.

13 C. Ding, Y. Zhang, F. Liu, Y. Kitabatake, S. Hayase, T. Toyoda, K. Yoshino, T. Minemoto, K. Katayama and Q. Shen, Effect of the conduction band offset on interfacial recombination behavior of the planar perovskite solar cells, *Nano Energy*, 2018, **53**, 17–26.

14 H. M. Pham, S. D. H. Naqvi, H. Tran, H. V. Tran, J. Delda, S. Hong, I. Jeong, J. Gwak and S. Ahn, Effects of the Electrical Properties of SnO2 and C60 on the Carrier Transport Characteristics of p-i-n-Structured Semitransparent Perovskite Solar Cells, *Nanomaterials*, 2023, **13**(24), 3091.

15 A. Bag, R. Pandey, S. Kashyap, J. Madan and J. Ramanujam, The influence of top electrode work function on the performance of methylammonium lead iodide based perovskite solar cells having various electron transport layers, *Chem. Phys. Lett.*, 2022, **806**, 140009.

16 T. Minemoto and M. Murata, Theoretical analysis on effect of band offsets in perovskite solar cells, *Sol. Energy Mater. Sol. Cells*, 2015, **133**, 8–14.

17 P. Caprioglio, M. Stolterfoht, C. M. Wolff, T. Unold, B. Rech, S. Albrecht and D. Neher, On the Relation between the Open-Circuit Voltage and Quasi-Fermi Level Splitting in Efficient Perovskite Solar Cells, *Adv. Energy Mater.*, 2019, **9**(33), 1901631.

18 J. Thiesbrummel, V. M. Le Corre, F. Peña-Camargo, L. Perdigón-Toro, F. Lang, F. Yang, M. Grischek, E. Gutierrez-Partida, J. Warby, M. D. Farrar, S. Mahesh, P. Caprioglio, S. Albrecht, D. Neher, H. J. Snaith and M. Stolterfoht, Universal Current Losses in Perovskite Solar Cells Due to Mobile Ions, *Adv. Energy Mater.*, 2021, **11**(34), 2101447.

19 W. Xu, L. J. F. Hart, B. Moss, P. Caprioglio, T. J. Macdonald, F. Furlan, J. Panidi, R. D. J. Oliver, R. A. Pacalaj, M. Heeney, N. Gasparini, H. J. Snaith, P. R. F. Barnes and J. R. Durrant, Impact of Interface Energetic Alignment and Mobile Ions on Charge Carrier Accumulation and Extraction in p-i-n Perovskite Solar Cells, *Adv. Energy Mater.*, 2023, **13**(36), 2301102.

20 L. J. F. Hart, F. J. Angus, Y. Li, A. Khaleed, P. Calado, J. R. Durrant, A. B. Djurišić, P. Docampo and P. R. F. Barnes, More is different: mobile ions improve the design tolerances of perovskite solar cells, *Energy Environ. Sci.*, 2024, **10**(1039), D4EE02669A.

21 S. Baumann, Stability and reliability of perovskite containing solar cells and modules: degradation mechanisms and mitigation strategies, *Energy Sci. Eng.*, 2024, **17**, 7566–7599.

22 S. G. McCallum, O. Nicholls, K. O. Jensen, M. V. Cowley, J. E. Lerpinière and A. B. Walker, Bayesian parameter estimation for characterising mobile ion vacancies in perovskite solar cells, *J. Phys. Energy*, 2024, **6**(1), 015005.

23 T. Kirchartz and B. Das, Transforming characterization data into information in the case of perovskite solar cells, *J. Phys. Energy*, 2023, **5**(3), 031001.

24 E. Von Hauff and D. Klotz, Impedance spectroscopy for perovskite solar cells: characterisation, analysis, and diagnosis, *J. Mater. Chem. C*, 2022, **10**(2), 742–761.

25 A. Guerrero, J. Bisquert and G. Garcia-Belmonte, Impedance Spectroscopy of Metal Halide Perovskite Solar Cells from the Perspective of Equivalent Circuits, *Chem. Rev.*, 2021, **121**(23), 14430–14484.

26 C. Gonzales, A. Guerrero and J. Bisquert, Transition from Capacitive to Inductive Hysteresis: A Neuron-Style Model to Correlate $I - V$ Curves to Impedances of Metal Halide Perovskites, *J. Phys. Chem. C*, 2022, **126**(32), 13560–13578.

27 A. J. Riquelme, K. Valadez-Villalobos, P. P. Boix, G. Oskam, I. Mora-Seró and J. A. Anta, Understanding equivalent circuits in perovskite solar cells. Insights from drift-diffusion simulation, *Phys. Chem. Chem. Phys.*, 2022, **24**(26), 15657–15671.

28 E. Ghahremanirad, O. Almora, S. Suresh, A. A. Drew, T. H. Chowdhury and A. R. Uhl, Beyond Protocols: Understanding the Electrical Behavior of Perovskite Solar Cells by Impedance Spectroscopy, *Adv. Energy Mater.*, 2023, **13**(30), 2204370.

29 W. Clarke, G. Richardson and P. Cameron, Understanding the Full Zoo of Perovskite Solar Cell Impedance Spectra with the Standard Drift-Diffusion Model, *Adv. Energy Mater.*, 2024, **14**(32), 2400955.

30 O. Almora, P. López-Varo, R. Escalante, J. Mohanraj, L. F. Marsal, S. Olthof and J. A. Anta, Instability analysis of perovskite solar cells via short-circuit impedance spectroscopy: A case study on NiOx passivation, *J. Appl. Phys.*, 2024, **136**(9), 094502.

31 A. Riquelme, L. J. Bennett, N. E. Courtier, M. J. Wolf, L. Contreras-Bernal, A. B. Walker, G. Richardson and J. A. Anta, Identification of recombination losses and charge collection efficiency in a perovskite solar cell by comparing impedance response to a drift-diffusion model, *Nanoscale*, 2020, **12**(33), 17385–17398.

32 L. J. Bennett, A. J. Riquelme, J. A. Anta, N. E. Courtier and G. Richardson, Avoiding Ionic Interference in the Computation of Ideality Factor for Perovskite Solar Cells and an Analytical Theory for Their Impedance Spectroscopy Response, *Phys. Rev. Appl.*, 2023, **19**, 014061.

33 M. Nabil, I. Grau, R. Grau-Crespo, S. Hamad and J. A. Anta, Inversion of the Impedance Response Towards Physical Parameter Extraction Using Interpretable Machine Learning, *Adv. Energy Mater*, 2026, **16**(20), e06352.

34 P. Calado, I. Gelmetti, B. Hilton, M. Azzouzi, J. Nelson and P. R. F. Barnes, Driftfusion: an open source code for simulating ordered semiconductor devices with mixed ionic-electronic conducting materials in one dimension, *J. Comput. Electron.*, 2022, **21**(4), 960–991.

35 J. Lim, M. Kober-Czerny, Y.-H. Lin, J. M. Ball, N. Sakai, E. A. Duijnstee, M. J. Hong, J. G. Labram, B. Wenger and H. J. Snaith, Long-range charge carrier mobility in metal halide perovskite thin-films and single crystals via transient photo-conductivity, *Nat. Commun.*, 2022, **13**(1), 4201.

36 S. Ravishankar, Z. Liu, U. Rau and T. Kirchartz, Multilayer Capacitances: How Selective Contacts Affect Capacitance Measurements of Perovskite Solar Cells, *PRX Energy*, 2022, **1**(1), 013003.

37 S. Ravishankar, T. Unold and T. Kirchartz, Comment on 'Resolving spatial and energetic distributions of trap states in metal halide perovskite solar cells, *Science*, 2021, **371**(6532), eabd8014.

38 A. Lasia, The Origin of the Constant Phase Element, *J. Phys. Chem. Lett.*, 2022, **13**(2), 580–589.

39 O. Almora, C. I. Cabrera, S. Erten-Ela, K. Forberich, K. Fukuda, F. Guo, J. Hauch, A. W. Y. Ho-Baillie, T. J. Jacobsson, R. A. J. Janssen, T. Kirchartz, M. A. Loi, X. Mathew, D. B. Mitzi, M. K. Nazeeruddin, U. W. Paetzold, B. P. Rand, U. Rau, T. Someya, E. Unger, L. Vaillant-Roca and C. J. Brabec, Device Performance of Emerging Photovoltaic Materials (Version 4), *Adv. Energy Mater.*, 2024, **14**(4), 2303173.

40 A. These, L. J. A. Koster, C. J. Brabec and V. M. Le Corre, Beginner's Guide to Visual Analysis of Perovskite and Organic Solar Cell Current Density–Voltage Characteristics, *Adv. Energy Mater.*, 2024, **14**(21), 2400055.

41 P. Würfel, and U. Würfel, "Chapter 6.4: The P-N Junction," in *Phys. Sol. Cells Basic Princ. Adv. Concepts*, 3rd edn, (Wiley-VCH Verlag GmbH & Co, 2016), pp. 132–145.

42 U. Rau, V. Huhn and B. E. Pieters, Luminescence Analysis of Charge-Carrier Separation and Internal Series-Resistance Losses in Cu (In , Ga) Se 2 Solar Cells, *Phys. Rev. Appl.*, 2020, **14**(1), 014046.

43 D. Grabowski, Z. Liu, G. Schöpe, U. Rau and T. Kirchartz, Fill Factor Losses and Deviations from the Superposition Principle in Lead Halide Perovskite Solar Cells, *Sol. RRL*, 2022, **6**(11), 2200507.

44 N.-P. Harder, Chapter 3: Recombination processes in real materials," in Exp. Theor. Investig. Second Third Gener. Photovolt. Devices, *PhD Thesis*, Leipzig University, 2006, pp. 65–82.

45 M. A. Torre Cachafeiro and W. Tress, Ionic Losses and Gains in Perovskite Solar Cells: Impact on Efficiency and Stability, *ACS Energy Lett.*, 2025, 4849–4855.

46 B. Tan, S. R. Raga, K. J. Rietwyk, J. Lu, S. O. Fürer, J. C. Griffith, Y.-B. Cheng and U. Bach, The impact of spiro-OMeTAD photodoping on the reversible light-induced transients of perovskite solar cells, *Nano Energy*, 2021, **82**, 105658.

47 A. Niemegeers and M. Burgelman, Effects of the Au/CdTe back contact on IV and CV characteristics of Au/CdTe/CdS/TCO solar cells, *J. Appl. Phys.*, 1997, **81**(6), 2881–2886.

48 J. Bisquert, Chemical capacitance of nanostructured semiconductors: its origin and significance for nanocomposite solar cells, *Phys. Chem. Chem. Phys.*, 2003, **5**(24), 5360.

49 P. Lopez-Varo, J. A. Jiménez-Tejada, M. García-Rosell, J. A. Anta, S. Ravishankar, A. Bou and J. Bisquert, Effects of Ion Distributions on Charge Collection in Perovskite Solar Cells, *ACS Energy Lett.*, 2017, **2**(6), 1450–1453.

50 D. Zhang, A. Allagui, A. S. Elwakil, Z. Yan and H. Lu, Active circuit model of low-frequency behavior in perovskite solar cells, *Org. Electron.*, 2020, **85**, 105804.

51 E. Ghahremanirad, A. Bou, S. Olyaee and J. Bisquert, Inductive Loop in the Impedance Response of Perovskite Solar Cells Explained by Surface Polarization Model, *J. Phys. Chem. Lett.*, 2017, **8**(7), 1402–1406.

52 D. Moia, I. Gelmetti, P. Calado, W. Fisher, M. Stringer, O. Game, Y. Hu, P. Docampo, D. Lidzey, E. Palomares, J. Nelson and P. R. F. Barnes, Ionic-to-electronic current amplification in hybrid perovskite solar cells: ionically gated transistor-interface circuit model explains hysteresis and impedance of mixed conducting devices, *Energy Environ. Sci.*, 2019, **12**(4), 1296–1308.

53 E. Ghahremani Rad, E. H. Balaguera, A. T. Gidey, K. Latosinsky, J. Bisquert and A. R. Uhl, Linking Double Inductance in Impedance Spectroscopy to Ionic Losses in Perovskite Photovoltaics, *ACS Energy Lett.*, 2026, **11**(4), 3211–3218.

54 E. H. Balaguera and J. Bisquert, Accelerating the Assessment of Hysteresis in Perovskite Solar Cells, *ACS Energy Lett.*, 2024, **9**(2), 478–486.

